Synthesis and properties of the NdSF compound, phase diagram of the NdF$_3$–Nd$_2$S$_3$ system

V.M. Grigorchenko [a,*], M.S. Molokeev [b,c], A.S. Oreshonkov [b,c], A.S. Aleksandrovsky [b,c], A.V. Kertman [a], M.U. Abulkhaev [a,f], A.S. Mereshchenko [f], I.O. Yurev [a], N.A. Shulaev [a], D.N. Kamaev [d], A.V. Elyshev [a], O.V. Andreev [a,e]

[a] *Tyumen State University, Tyumen, Volodarsky str. 6, 625003, Russia*
[b] *Kirensky Institute of Physics, Federal Research Center KSC SB RAS, Krasnoyarsk, Akademgorodok str. 50, Building 38, 660036, Russia*
[c] *Siberian Federal University, Krasnoyarsk, Svobodnyj av. 79, 660079, Russia*
[d] *Department of Physical and Applied Chemistry, Kurgan State University, Sovetskaya str. 63/4, Kurgan, 640020, Russia*
[e] *Institute of Solid State Chemistry, Ural Branch, Russian Academy of Sciences, Yekaterinburg, Pervomaiskaya str. 91, 620990, Russia*
[f] *Saint-Petersburg State University, 7/9 Universitetskaya Emb., 199034, St. Petersburg, Russia*

ARTICLE INFO

ABSTRACT

The NdF$_3$–Nd$_2$S$_3$ system attracts attention of researchers due to the possibility of using LnSF compounds (Ln = rare earth element) as possible new *p*- and *n*-type materials. The samples of this system were synthesized from NdF$_3$ and Nd$_2$S$_3$. The NdSF compound belongs to the PbFCl structural type, *P4/nmm* space group, unit cell parameters: a = 3.9331(20) Å, c = 6.9081(38) Å. The experimentally determined direct and indirect NdSF bandgaps are equal to 2.68 eV and 2.24 eV. The electronic band structure was calculated via DFT simulation. The NdSF compound melts congruently at T = 1385 ± 10°C, ΔH_m = 40.5 ± 10 kJ/mol, ΔS = 24.4 ± 10 J/mol. The NdSF microhardness is 455 ± 10 HV. Five phase transformations in the NdF$_3$–Nd$_2$S$_3$ system were recorded by DSC; their balance equations were derived. The liquidus of the system calculated from the Redlich–Kister equation is fully consistent with the DSC data.

1. Introduction

The LnSF and LnSeF compounds (Ln is a rare earth element) are considered to be promising *p*- and *n*-type materials [1,2]. The LnSF compounds (1LnF$_3$: 1Ln$_2$S$_3$) are easy to prepare; they do not form noticeable regions of solid solutions with LnF$_3$ and Ln$_2$S$_3$ components and are chemically inert and thermally stable up to the melting temperatures [3].

The LnSF compounds are also promising optical materials [4–6]. Their optical band gaps are Eg = 2.77 eV for GdSF [3,4] and Eg = 2.81 eV for LaSeF [5]. The LnSF compounds exhibit a wide range of colors and have been patented as UV-resistant pigments [6–10].

The *Meta*-GGA band structure simulations predict a 1.481 eV direct bandgap for GdSF and agree well with experimental absorption features. The experiments were complemented by crystal structure predictions for LaSeF, which were performed by means of full geometry optimization using empirical potentials and local ab initio energy minimizations. The

calculation results agree with the observed structures and predict yet unknown LaSeF polymorphs. The electronic properties were studied experimentally and theoretically and demonstrated the possibility of bandgap engineering for LaSeF compounds [3,5].

The NdSF compound belongs to the PbFCl tetragonal structural type, *P4/nmm* space group, with the following unit cell parameters: a = 3.9278(1) Å, c = 6.9056(2) Å [11], a = 3.9264 (3) Å, c = 6.9058(5) Å [12].

Neodymium trifluoride belongs to the LaF$_3$ tysonite structural type, hexagonal crystal system, *P6$_3$/mcm* space group, Z = 6, with the following unit cell parameters: a = 7.025 Å, c = 7.199 Å [13], a = 7.018 Å, c = 7.183 Å [14]. The congruent melting temperature is 1377°C, ΔH = 53.7 kJ/mol [15].

The α-Nd$_2$S$_3$ low-temperature modification belongs to the α-La$_2$S$_3$ structural type, orthorhombic crystal system, *Pnma* space group, with the following unit cell parameters: a = 7.4397(5) Å, b = 4.0278(3) Å, c = 15.5196(1) Å [16]. The α-Nd$_2$S$_3$→γ-Nd$_2$S$_3$ transition temperature is
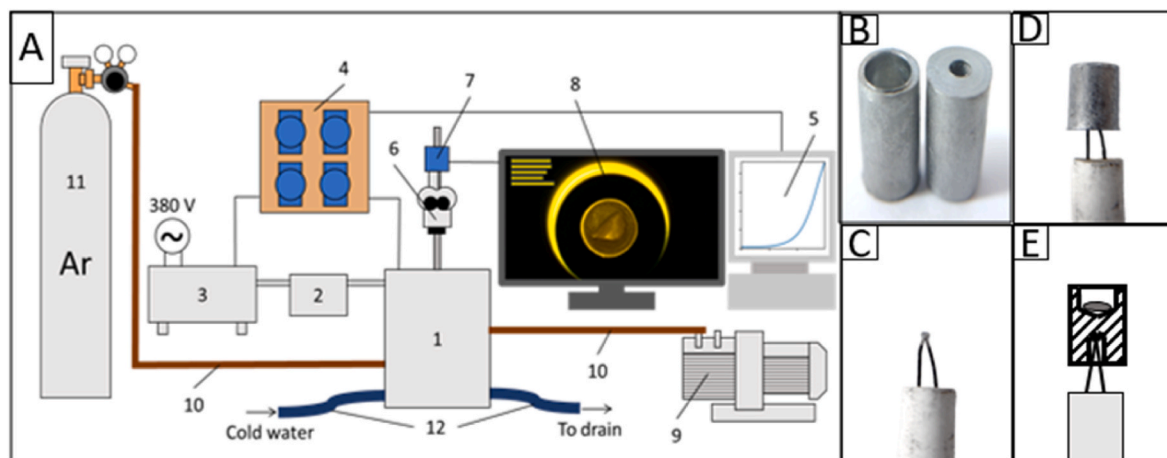

Fig. 1. Schematic of VTA-T setup and molybdenum crucibles. The setup (A) consists of several main units: working chamber (1), transformer (2), RIF-101 temperature controller (3), setup control and data acquisition unit (4) (I/O system made of ADAM 4000 series modules), personal computer (5), optical microscope (6), MC-HD-5 video camera (7), observation display (8), gas pump (9), gas hoses (10), inert gas balloon (11), coolant hoses (12). External view of molybdenum crucibles (B); thermocouple (C) with the crucible placed (D); schematic representation of the relative position of the thermocouple, crucible and sample (E).

1183°C [15]. The γ-Nd$_2$S$_3$ modification belongs to the Th$_3$P$_4$ structural type, $I\bar{4}3d$ space group, $a = 8.525$ Å [16]. Nd$_2$S$_3$ melts congruently at 1801°C, ΔH = 56.3 kJ/mol [17]. The particles of γ-Nd$_2$S$_3$ and α-Nd$_2$S$_3$ samples demonstrate a qualitatively similar morphology. The samples consist of spherical elongated particles forming intergrowths and agglomerates [16,17].

For cerium subgroup lanthanides, the LnSF compounds melt congruently. The NdSF compound is characterized by T$_m$ = 1381 ± 7°C and ΔH = 40.2 ± 4.0 kJ/mol [4].

It is quite a reasonable approach to combine experimental studies of phase diagrams with calculation methods, particularly liquidus line simulations using the Redlich–Kister equation. The liquidus lines calculated by this equation for various types of phase diagrams and chemical systems agree with the experimental data [3,17,18].

In this work, the optical and thermal properties of NdSF were studied, the electronic structure of this compound was determined, and the phase diagram of the NdF$_3$–Nd$_2$S$_3$ system was constructed.

2. Experimental methods

Synthesis of the samples. The following initial materials were used: neodymium oxide (99.998 mol. % Nd$_2$O$_3$), ammonium thiocyanate (98.9 mol. % NH$_4$SCN, SUOYI, China), ammonium fluoride (98.9 mol.% NH$_4$F), gaseous argon (99.999 % Ar, Himreactiv, Russia).

The NdF$_3$ and Nd$_2$S$_3$ samples were synthesized according to standard procedures. Neodymium trifluoride was prepared hydrothermally by autoclaving neodymium(III) nitrate in the presence of NH$_4$F at 120–180°C [19–21]. The obtained neodymium trifluoride powder was dried at 50 °C, and then the sample was annealed at 370 °C in the atmosphere of ammonium fluoride decomposition products to remove adsorbed water molecules and OH groups. The resulting NdF$_3$ compound belongs to the LaF$_3$ structural type, $P6_3/mcm$ space group, $a = 7.008(9)$ Å, $c = 7.178(6)$ Å. Neodymium trifluoride was kept in a desiccator at a residual air pressure of 1000–2000 Pa.

The Nd$_2$S$_3$ sample was synthesized by exposing Nd$_2$O$_3$ to a flow of H$_2$S and CS$_2$ at 1050–1100°C [22]. H$_2$S and CS$_2$ were prepared by thermal decomposition of NH$_4$CNS at 260–270°C [23]. The obtained α-Nd$_2$S$_3$ modification belongs to the orthorhombic system, α-La$_2$S$_3$ structural type, $Pnma$ space group, $a = 7.440$ Å, $b = 4.028$ Å, $c = 15.519$ Å. The cubic γ-Nd$_2$S$_3$ modification prepared by annealing the α-Nd$_2$S$_3$ modification in sulfur vapors at 1200–1300 °C belongs to the Th$_3$P$_4$ structural type, $a = 8.529$ Å [17,24,25].

In the NdF$_3$–Nd$_2$S$_3$ system, 22 samples of various chemical compositions were synthesized. Weighed amounts of initial NdF$_3$ and Nd$_2$S$_3$ substances were ground in an agate mortar and placed in a graphite crucible inside in a quartz ampoule. The ampoule was evacuated to 0.1 Pa and sealed. The sample was melted by heating the graphite crucible in a high-frequency current setup. The moment of melting was observed visually. The sample was kept in the melt for up to 2–3 min; then the sample was crystallized from the melt. The melting–crystallization cycles were repeated three to four times. The ampoules with the samples were annealed in a muffle furnace at 900 ± 5 °C for up to 500 h.

Research methods. The powder XRD analysis was carried out on a DRON-7 diffractometer (CuK$_\alpha$ radiation; Ni-filter; 2θ step: 0.02°; counting time per point: 2 s). The unit cell parameters were determined using the PDWin 4.0 package and the PDF-4 X-ray card file by means of X-ray diffraction profiling. The unit cell parameters were determined with an accuracy of ±0.0001 nm [26–35]. Therefore, this structure was utilized as the starting model for the Rietveld refinement, which was performed using the TOPAS 4.2 program [36,37].

The differential scanning calorimetry (DSC) study was performed on a SETARAM Setsys Evolution (TGA–DSC 1600) analyzer equipped with a PtRh6%-PtRh30% thermocouple using the SETSOFT 2000 data processing software. The 50 mg samples were kept in graphite crucibles. The measurements were carried out in an argon flow supplied to the upper part of the chamber at a rate of 20 mL/min. The samples were heated at a rate of 10 K/min. The temperature and enthalpy of phase transformations were determined with an accuracy of ±1.8 K and ±7%, respectively [3,18,38,39].

The visual thermal analysis (VTA) was carried out on an original VTA-T setup (Fig. 1 A).

For VTA, a 50 mg polycrystalline sample was placed in a 10 mm high molybdenum crucible (5 mm in diameter) having two holes on its opposite flat ends (Fig. 1 B). The crucible was placed on a WRe 5/20 thermocouple (Fig. 1 C), the lower hole downwards (Fig. 1 D, 1 E), on the graphite heater axis. The sample was loaded through the upper hole. The setup was evacuated and filled with argon to a pressure of 1.1 bar. The heating rate varied from 20 to 500 °C/min. The state of the sample was monitored and recorded using an MC-HD-5 video camera. The setup was calibrated for the following melting points: Cu (1085 °C), Ni (1455 °C), Pd (1555 °C), Pt (1738 °C), white sapphire (2050 °C). The calibration was performed with a reliability level of 98%. The temperatures were determined with an accuracy of 0.5–1.0% of their value. The eutectic melting temperature was determined by the appearance of a distinct liquid phase in the sample. The melts of the samples were
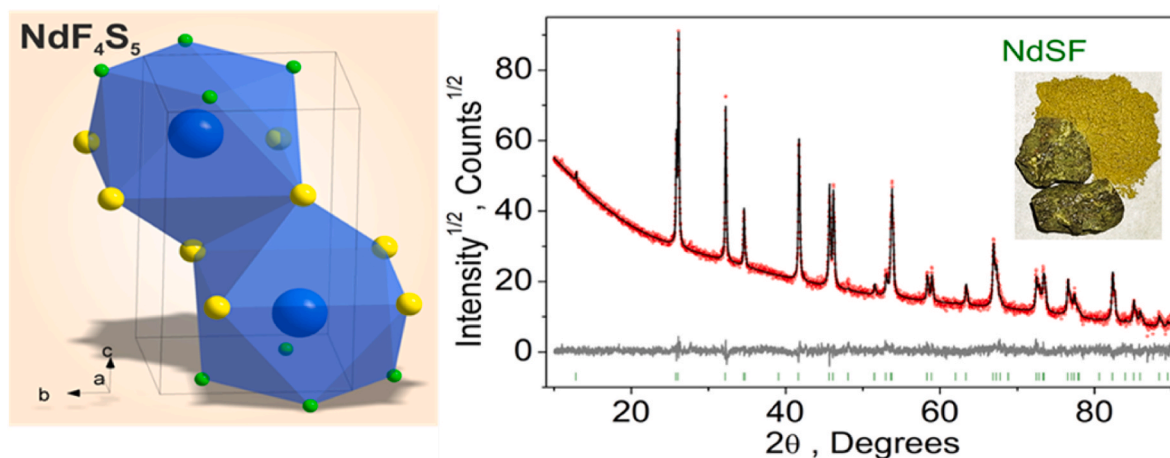
Fig. 2. Crystal structure of NdSF and the Rietveld difference plot for this compound.

transparent in the visible region: the bottom of the crucible was clearly seen, and its reflection in the form of a round spot appeared on the sample surface. The liquidus temperature was determined as the point when the melt became transparent [40].

The chemical composition of the phases was determined using an Oxford instruments X-Max energy-dispersive analyzer as part of the Tescan Mira 3 LMU device [17]. For each sample, the element contents were obtained at 6–9 points. The contents deviating more than by 7% were considered to be misses and were not considered. The remaining values were averaged and processed using Student's t-distribution for a coefficient of 0.97.

The microstructural analysis (MSA) of polished and etched thin sections of the samples was conducted on an AxioVert A1 MAT metallographic microscope using the AxioVision SE64 software [17,40].

The microhardness of polycrystalline samples was determined on a HMV-G21DT tester at a load of 490.3 mN (50 g) using the implemented device software.

The UV diffuse reflectance spectra of thin powder layers were recorded in the range of 200–1400 nm using a Shimadzu UV-2600 spectrophotometer (Japan) equipped with an ISR-2600 Plus integrating spherical attachment [41]. The spectra were recorded with respect to the $BaSO_4$ standard (supplied by Shimadzu with the spectrophotometer) and processed using the Kubelka–Munk function, which was modified for the cases of direct and indirect interband transitions [42,43]. After constructing a linear approximation for the fundamental absorption region, the linearity regions were chosen in such a way that the Pearson correlation coefficient was equal to 0.999 (e.g., like in the work by Rampino [42]).

The Fourier-transform infrared spectroscopy (FTIR) analysis was carried out on a FSM 1201 FTIR spectrometer. The sample was prepared in the form of KBr pellets.

The Raman spectra were recorded on an i-Raman Plus spectrometer using 785 nm laser excitation.

2.1. Calculation details

The density functional theory calculations were carried out using the CASTEP (Cambridge Serial Total Energy Package) [44] code. The meta-generalized gradient approximation with the on-site orbital dependent Hubbard U energy term [45] and the RSCAN functional [46] were used. For the Nd 4*f* orbital, the U value was taken equal to 6 eV. On-the-fly generated ultrasoft pseudopotentials with a cutoff energy of 650 eV were used. The Brillouin zone was sampled by a $5 \times 5 \times 3$ Monkhorst–Pack *k*-mesh. The experimental geometry of the NdSF crystal was optimized using the *meta*-GGA method until a maximum force of 0.01 eV/Å and a maximum stress of 0.02 GPa. The total energy

minimization was performed according to the convergence criterion of 1×10^{-7} eV.

The presented form of equation (1) was used. The equations were prepared for characteristic phase equilibria in the system. Data on the melting enthalpies of pure solid components were taken from sources [17,47] and experimental data. When solving the mathematical system of equations, the numerical coefficients in the Redlich-Krister equation were found. Knowing the numerical coefficients, the liquidus temperature was considered as a function of composition. This approach has proved satisfactory in the study of state diagrams of various systems [3, 18,47].

$$\frac{\Delta H(T_m - T)}{T_m} = -\left[RT\ln x_1 + (1 - x_1)^2\left[L_0 + L_1(4x_1 - 1) + L_2(12x_1^2 - 8x_1 + 1)\right]\right]$$

(1)

3. Results and discussions

3.1. Crystal chemical parameters of NdSF. Phase equilibrium in the NdF₃–Nd₂S₃ system

The XRD pattern of the NdSF compound (CSD-2324320) was solved in the tetragonal system, PbFCl structural type, *P4/nmm* space group, in

Table 1

Crystal data and structure refinement for NdSF.

Compound	NdSF
Space group	*P4/nmm*
a (Å)	3.9331(2)
c (Å)	6.9081(4)
V (Å³)	106.862(12)
Z	2
2θ range for data collection, °	10–90
R_{wp},%	6.02
R_p,%	4.1
χ^2	1.56
R_B,%	2.33

Table 2

Fractional atomic coordinates and isotropic displacement parameters (Å²) for NdSF.

Atom	*x*	*y*	*z*	B_{iso}	*Occ.*
Nd	0.25	0.25	0.2296(2)	0.5(3)	1
S	0.25	0.25	0.6456(9)	2.0(3)	1
F	0.75	0.25	0	1.8(5)	1

Table 3
Main bond lengths (Å) in NdSF.

Nd—S^i	2.9117(18)	Nd—S^{ii}	2.874(6)
Nd—F	2.526(1)		

Symmetry codes: (i) *-x, -y, -z+1*; (ii) *-x+1/2, -y+1/2, z*.

agreement with the data reported in Ref. [11]. The neodymium atom is located in the center of a capped square antiprism and is surrounded by five sulfur atoms and four fluorine atoms (Fig. 2, Tables 1 and 2).

The NdSF crystals and powder are yellow-greenish in color (Fig. 2).

The La^{3+} site was occupied by the Nd^{3+} ion (Fig. 2). The refinement was stable, and the obtained *R*-factors were small (Table 1, Fig. 2). The atomic coordinates and main bond lengths are listed in Tables 2 and 3, respectively.

When the substances occur in the polycrystalline state for 0–50 mol. % Nd$_2$S$_3$ concentrations in the NdF$_3$–Nd$_2$S$_3$ system, the NdF$_3$ and NdSF phases exist in equilibrium. For 50–100 mol.% Nd$_2$S$_3$ concentrations, the NdSF and γ-Nd$_2$S$_3$ phase states were registered upon annealing and cooling the samples. As a result of annealing at 900 °C, the samples adopted the NdSF + α-Nd$_2$S$_3$ phase composition. In the system based on NdF$_3$, NdSF, and α-Nd$_2$S$_3$ compounds, no noticeable solid solutions were formed. Within the measurement error, the unit cells parameters of each phase in the two-phase samples coincided with those of the single-phase samples of these compounds.

3.2. Simulation of NdSF geometry and electronic structure

Recently, ab initio simulation of LnSF crystals we performed in the work by Prof. Demourges et al. [48], where a modified DFT method with a modified Becke-Johnson exchange-correlation potential were used. The simulated and experimental bandgap values were compared by finding the energy difference between the conduction band bottom and the valence band top. According to Prof. Demourgues, the conduction band bottom in LnSF is formed by a single branch, characterized by strong dispersion. In our later work [3] we used the *meta*-GGA RSCAN functional for GdSF and obtained a different result. We showed that in the case of strong dispersion, a formally direct interband transition contributes to the indirect bandgap. Two indirect bandgaps were detected in GdSF to be equal to 1.54 and 2.4 eV. In the present article, we develop this approach, which was previously tested for GdSF, for the case of NdSF. We will show that fitting the simulation to make the energy difference between the conduction band bottom and the valence

band top coinciding with the experimental bandgap is not the best strategy. A more attractive approach implies the fitting of the simulated absorption curve to the experimental Kubelka-Munk Function.

At the first step of DFT calculations, the geometry was optimized using the initial structural data from Tables 1 and 2 The obtained lattice parameters *a* and *c* are equal to 3.98 Å and 7.00 Å, respectively. The discrepancy with experimental data was less than 1.2 % for *a* and less than 1.4 % for *c*. The optimized *z* coordinates of Nd and S differ only in the third decimal place, their values being equal to 0.22848 and 0.64863, respectively. Thus, the NdSF geometry calculated in the *meta*-GGA RSCAN approximation agrees well with the experimental data.

Fig. 3 shows the calculated electronic structure. Fig. 3 *a* presents the band structure with highlighted indirect electronic transitions, while Fig. 3 *b* shows direct transitions. Since neodymium is a lanthanide element, the spin up and spin down states are shown in black and red colors, respectively. The path through high-symmetry points of the Brillouin zone is the same as the one used in Ref. [3]. As can be seen in Fig. 3 *a*, the following indirect electronic transitions can be distinguished for the spin up case (those for the spin down case are shown in parentheses): Γ–Z 1.64 (2.2), Z–Γ 2.13 (2.78), and Z–Γ 2.57 (2.98) eV. According to Fig. 3 *b*, the following marked direct transitions can be distinguished for the spin up case (those for the spin down case are shown in parentheses): Γ–Γ 1.58 (2.134), Z–Z 2.19 (2.84), Z–Z 2.63 (3.051), and Γ–Γ 3.27 (3.76) eV. Fig. 3 contains also other indirect and direct high-energy electronic transitions, but we do not consider them in this work. The comparison of the band structure calculated by Prof. Demourgues with that obtained in our study shows that the band shapes are similar in both cases. The differences are as follows: 1) bandgap sizes 2) positions of excited states originating from unoccupied f orbitals of individual Nd ions. The latter can hardly influence the bandgap due to the weakness of the ff absorption. The former, as will be shown below, can be useful for the correct bandgap determination. Finally, note that the lowest subbands in the conduction band show strong dispersion, like in the case of GdSF [3], possibly manifested as similar features of the Kubelka–Munk function.

Fig. 4 images the total density of states (DOS) and partial densities of states (PDOS). Unfortunately, we could find no XPS data for these compounds and therefore could not compare the valence band positions, as it was earlier done for GdSF in work [3] where a good agreement was reported. According to Fig.4, the top of the NdSF valence band is formed by S *p*-states, while the bottom of its conduction band is mainly formed by Nd *d*-states.
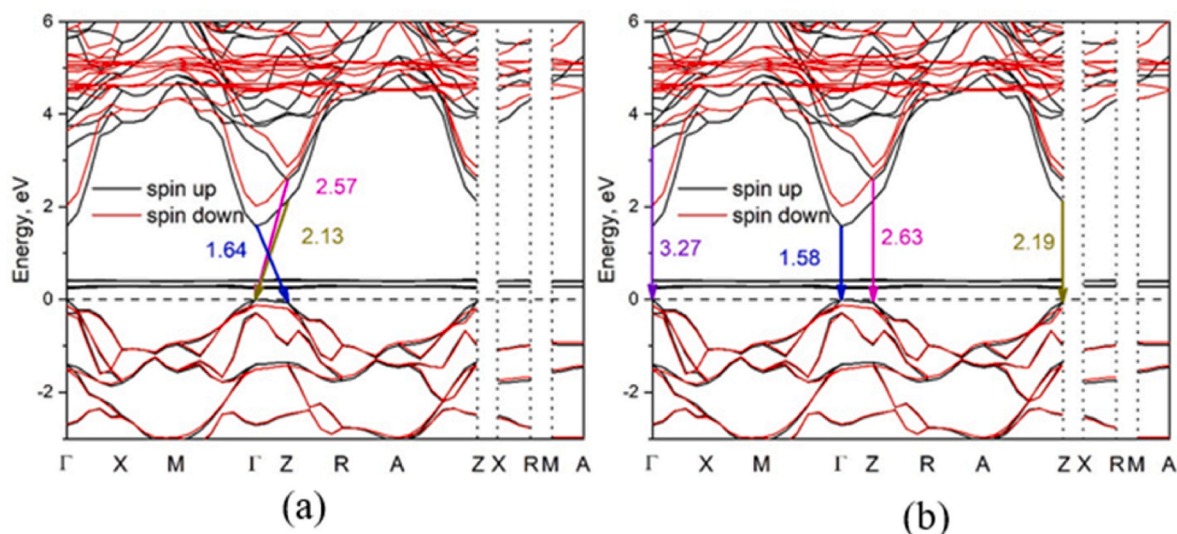

Fig. 3. Electronic band structure of NdSF calculated using the *meta*-GGA RSCAN method: indirect transitions (a), direct transitions (b).
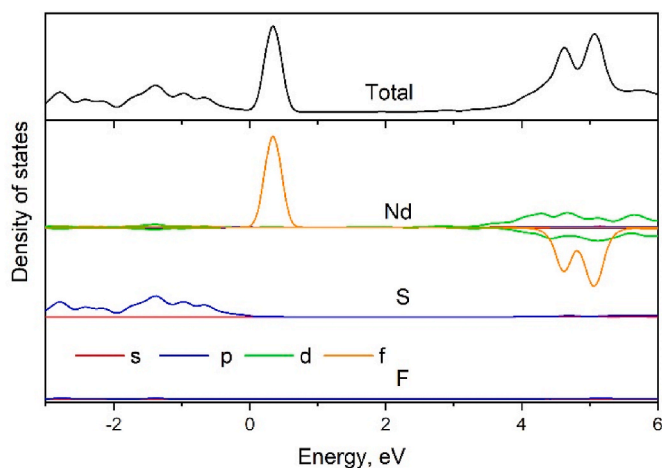
Fig. 4. Total and partial densities of states in NdSF.

3.3. Diffuse reflectance spectra and optical bandgap of NdSF

Fig. 5 shows the Kubelka–Munk functions derived from the NdSF diffuse reflectance spectra and modified for the goal of determining direct and indirect optical bandgaps. The direct and indirect NdSF bandgaps are equal to 2.68 eV and 2.24 eV, respectively. However, before the beginning of the fundamental indirect bandgap absorption, there is one more distinct linear part of the Kubelka–Munk function corresponding to a smaller optical bandgap of 1.3 eV (Fig. 5, top). These features are very close to the result that was recently reported for the GdSF crystal [3]. In fact, the GdSF direct bandgap was found equal to 2.77 eV, and two indirect bandgaps were determined as 2.4 eV and 1.54 eV. The following highly interesting feature was revealed by comparing the experimental data obtained for GdSF with the corresponding DFT data: the formally direct bandgap was predicted at 1.481 eV; however, the calculations suggest that this interband transition is related (due to high dispersion) to an indirect bandgap. The absorption spectrum calculations showed that the real onset of direct bandgap in GdSF occurs above 2.5 eV, in agreement with the experiment.

In view of interesting results obtained for the GdSF bandgaps, it is a worthy task to compare the experimental and simulated spectra of other LnSF crystals. NdSF can be used for such comparison, though it is a more difficult object for computer simulations than GdSF. It is well-known that the DFT approach suffers from errors due to the interaction between f electrons. For instance, the smallest errors will be obtained in DFT calculations involving the Ce^{3+} ion, which has only one f electron. The errors will be minimal also in the case of Gd^{3+} ions possessing seven outer-shell $4f$ electrons, corresponding to a half-filled f-shell. The Nd^{3+} ion has three $4f$ electrons and is expected to be the most difficult object for DFT calculations.

Fig. 5 (top) shows that the DFT calculations predict several spectral features in the vicinity of the indirect bandgap. Between 1 eV and 2 eV, the calculated curve contains a contribution of f-f transitions. The onset of fundamental absorption above 2 eV, resulting in the experimental indirect bandgap of 2.4 eV, is also predicted. In contrast to GdSF, no small indirect bandgap $E_{g\ ind1}$ equal to 1.3 eV was found because of the superposed f-f contribution. As can be seen from Fig. 5 (below), the onset of fundamental absorption at the direct bandgap is less correct than in the case of indirect bandgap in NdSF or in the case of GdSF.

3.4. Morphology of the compound particles. Microstructure of the samples of the NdF_3–Nd_2S_3 system

The particles of synthesized NdF_3, NdSF, and α-Nd_2S_3 samples exhibit different morphologies. The NdF_3 powder (Fig. 6 A) consists of oval 9–12 µm agglomerates formed by spherical 0.3–1 µm grains. The
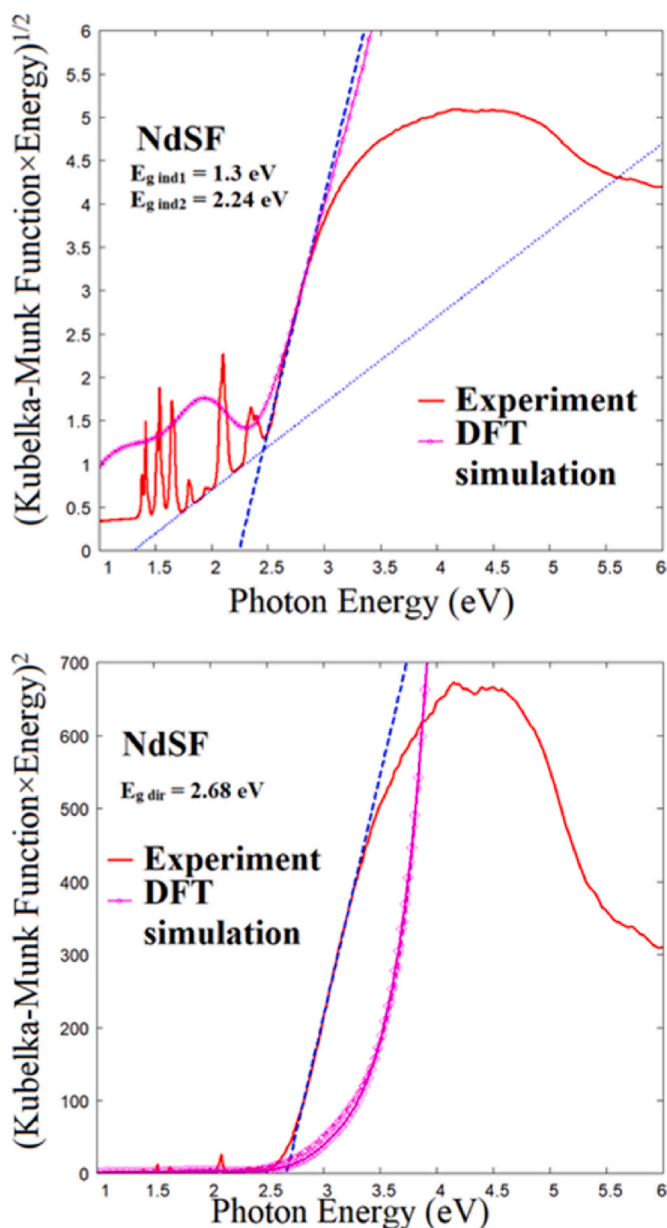

Fig. 5. Kubelka–Munk functions of NdSF for indirect (top) and direct (bottom) bandgaps as compared with the DFT calculated absorption spectra.

NdSF particles (Fig. 6 B) have a layered structure. The planes and edges of the crystals are clearly visible, some of them characterized by formed cuttings. The 7–20 µm α-Nd_2S_3 particles (Fig. 6 C) have elongated cylindrical shapes; the sintered particles form an openwork structure.

The chemical composition of the samples was determined by EDS. For the NdF_3 powder, the Nd and F contents in the sample were confirmed only qualitatively, and their values are shown in parentheses (Fig. 6 A). For the NdSF powder, the determined contents of chemical elements generally coincide with those calculated from the chemical formula (Fig. 6 B). For the Nd_2S_3 powder, only the Nd and S contents were close to the calculated ones. The coincidence of calculated and established contents of chemical elements in NdSF is due to the fact that the studies were conducted with flat crystal faces. The particles of NdF_3 and Nd_2S_3 powders have oval surfaces and therefore do not meet the requirements set by the EDS method for the accurate elemental content measurements.

The impurities are oxygen and aluminum. Oxygen is an impurity element due to the contact with the atmosphere; aluminum is a
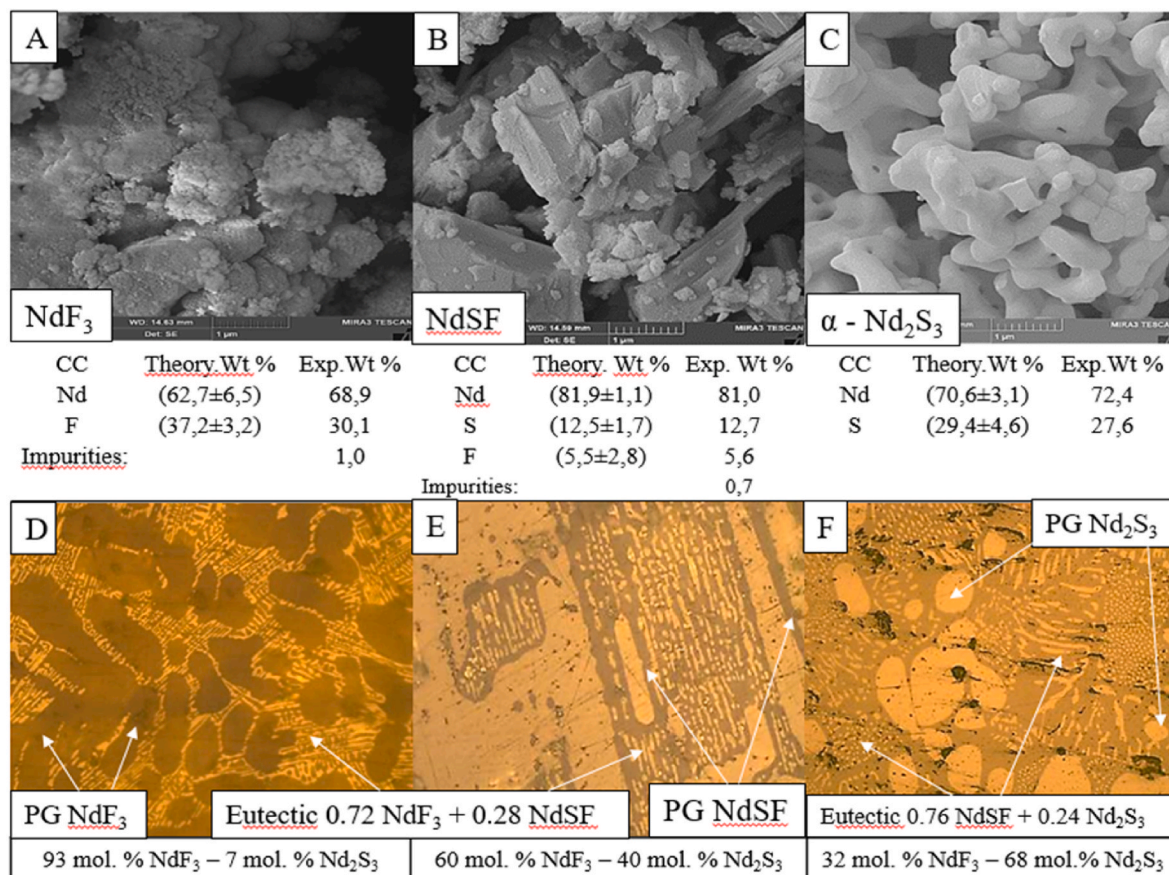
Fig. 6. SEM images of NdF_3 (A), NdSF (B), and Nd_2S_3 (C) particles. The chemical composition according to the SEM data is presented under the images. Microstructures of the thin sections of melt-grown samples of the NdF_3–Nd_2S_3 system (D, E, F). Phase compositions are indicated in the captions. The PG abbreviation denotes primary grains.

Table 4
Microhardness of phases NdF_3, NdSF, Nd_2S_3 in NdF_3–Nd_2S_3 system samples.

Phase	Microhardness, HV	Microhardness NdF_3, NdSF, Nd_2S_3, in two-phase samples, HV				
NdF_3	345 ± 20	343	367	–	–	–
NdSF	455 ± 10	–	–	445	455	–
Nd_2S_3	700 ± 15	–	–	–	–	711
Compositions of two-phase samples in mol.% Nd_2Se_3		7	12	40	50	75

background element, since its peak occurs during the calibration.

The microstructure data obtained for the thin sections of samples of the NdF_3–Nd_2S_3 system completely coincide with the XRD data. The sample containing 7 mol. % of Nd_2S_3 is formed by NdF_3 primary grains and by the 0.72 NdF_3 + 0.28 NdSF eutectic (Fig. 6 D). The oval shape of NdF_3 primary grains is similar to the shape of grains in the NdF_3 crystals (Fig. 6 A). In the 40 mol.% Nd_2S_3 sample, rectangular NdSF primary grains were formed (Fig. 6 E), their shape being similar to that of NdSF particles (Fig. 6 B). A correlation was also observed between oval Nd_2S_3 particles and oval primary grains of Nd_2S_3 crystals in the 68 mol. % Nd_2S_3 sample (Fig. 6 F). Both eutectics in Fig. 6 D, E, F are formed by elongated grains of equilibrium phases. In Fig. 6 F, the axial and transverse sections of eutectic grains can be clearly seen.

Within the measurement uncertainty, the same phase in various samples with different phase compositions exhibits similar microhardness (Table 4). The microhardness of the phases naturally increases in the NdF_3 – NdSF – Nd_2S_3 series.

3.5. NdSF thermal characteristics. Phase transformations in the NdF_3–Nd_2S_3 system

Five phase transformations were detected by DSC in the NdF_3–Nd_2S_3 system. According to the DSC data, the melting enthalpies and melting points of NdF_3 almost coincide with the calorimetric data [15] (Fig. 7 A, Table 5 No. 1).

The melting peak of the 0.72NdF_3–0.28NdSF eutectic on the state diagram has a distinct linear region, fully corresponding to the invariant eutectic equilibrium of the system. The DSC curve of the 25 mol. % Nd_2S_3 sample also shows peaks corresponding to complete melting and crystallization points, determining positions of the liquidus line (Fig. 7 B, C, Table 5 No. 2). The NdSF compound melts congruently. The DSC curve has a peak corresponding to the endothermic effect of melting of the NdSF sample (Fig. 7D–Table 5 No. 3).

Thermal stability of the NdSF compound is evidenced by the absence of noticeable mass losses on the TG curve.

The temperature of the 0.76 NdSF +0.24 Nd_2S_3 eutectic is only 10 °C lower than the melting point of NdSF (Fig. 7F–Table 5, No. 4). The flat shape of the peak corresponding to the NdSF melting indicates that the compound dissociates significantly in the melt [4]. The melting enthalpies of each eutectic as a whole is equal to the sum of melting enthalpies of their components calculated from the eutectic composition. The characteristics of the α-Nd_2S_3→γ-Nd_2S_3 polymorphic transition coincide with the literature data (Table 5, No. 5).

3.6. Phase diagram of the NdF_3–Nd_2S_3 system

The phase diagram of the NdF_3–Nd_2S_3 system was constructed. A
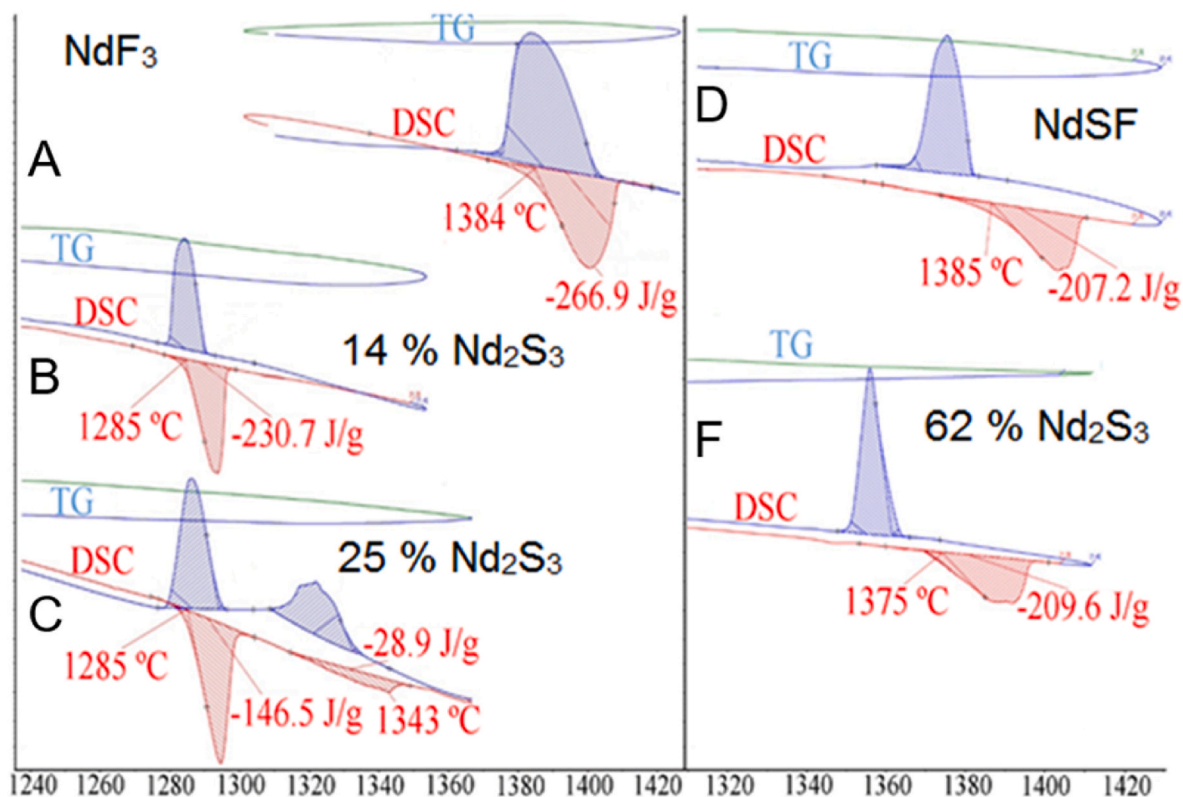
Fig. 7. DSC curves of the samples of the NdF_3–Nd_2S_3 system. Compositions of the samples in mol. % Nd_2S_3 are indicated.

Table 5
Temperatures, enthalpies, and entropies of phase transformations in the NdF_3–Nd_2S_3 system.

No	Phase transformation	Coordinates		Equation of the phase transformation	ΔH, J/g	ΔH, KJ/mol.	ΔS J/mol
		Composition	T, °C				
1	Congruent melting	NdF_3	1384 ± 2	$NdF_3 \leftrightarrows liquid$	266.9 ± 10 271.8 ± 10 [1]	53.7 ± 10	32.4 ± 10
2	Melting eutectic	14 mol.% Nd_2S_3	1285 ± 2	0.72 NdF_3 + 0.28 NdSF $\leftrightarrows$ liquid	230.7 ± 5	12.4 ± 5	8.0 ± 5
3	Congruent melting	NdSF	1385 ± 2	NdSF $\leftrightarrows$ liquid	207.2 ± 10 206.0 [2]	40.5 ± 10	24.4 ± 10
4	Melting eutectic	62 mol.% Nd_2S_3	1375 ± 2	0.76 NdSF + 0.24 Nd_2S_3 $\leftrightarrows$ liquid	209.6	50.0	30.3
5	Polymorphic transition	Nd_2S_3	1179 ± 5 1183 ± 2 [1]	α-$Nd_2S_3 \rightarrow \gamma$-$Nd_2S_3$	18.0 ± 3 19.6 ± 2 [1]	6.9 ± 3	4.8 ± 3

congruently melting NdSF compound is formed in the system. The NdSF compound divides the system into two eutectic-type subsystems: NdF_3–NdSF and NdSF–Nd_2S_3.

The liquidus of the system consists of four branches. The liquidus line of the system was calculated from the Redlich–Kister equation by writing down the equilibrium equations at the following phase equilibria: NdF_3 polycrystalline phase – eutectic melt (1); eutectic melt – NdSF polycrystalline phase (2); NdSF polycrystalline phase – melt (3); NdSF polycrystalline phase – eutectic melt (4); eutectic melt – Nd_2S_3 polycrystalline phase (5). For each of the five phase equilibria, we wrote the Redlich–Kister equation with substituted NdF_3, NdSF, Nd_2S_3 melting temperatures and enthalpies. A system of five mathematical equations was obtained by solving which obtained the following values of numerical coefficients: $L_0 = -27730$, $L_1 = 5836$, $L_2 = -16880$ [18]. The temperature of the liquidus line was calculated from these coefficients as a function of composition (Fig. 8). The DSC data for the liquidus temperatures agree with the position of the calculated liquidus line with a correlation coefficient of 0.99.

Since the constructed phase diagram of the NdF_3–Nd_2S_3 system noncontradictory incorporates the results obtained by independent methods, it can be considered a reliable one.

4. Conclusion

The obtained single-phase NdSF sample is characterized by the tetragonal crystal system, PbFCl structural type, *P4/nmm* space group. The resulting lattice parameters *a* and *c* are 3.9331(20) Å and 6.9081 (38) Å. The optimized *z* coordinates of Nd and S differ only in the third decimal place and are equal to 0.22848 and 0.64863, respectively. The experimental values of direct and indirect NdSF band gaps are 2.68 eV and 2.24 eV. The additional indirect band gap has a width of 1.3 eV.

The particles of the synthesized samples have the following morphology: agglomerate-forming spherical grains (NdF_3); layered structure, faceted crystals (NdSF); cylindrical ovals forming an open-work structure (α-Nd_2S_3). The shape of the particles correlate with that of the melt-grown crystals of the phases. The microhardness of the phases was determined. Each phase has the same microhardness in all samples with different phase compositions.

Five phase transformations were detected by DSC in the NdF_3–Nd_2S_3 system. The NdSF compound melts congruently. The compositions,
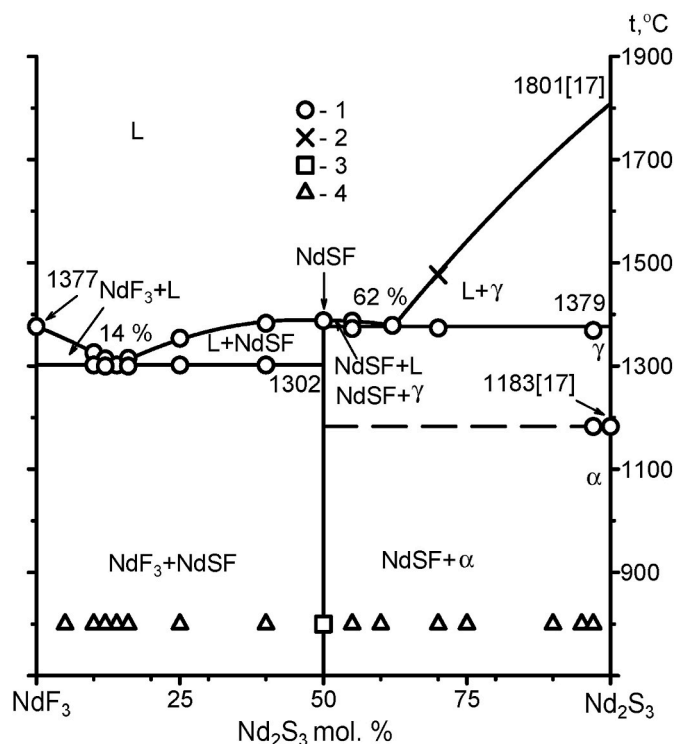
Fig. 8. Phase diagram of the NdF_3–Nd_2Ssystem: DSC data (1), VTA data (2). Phase composition of the samples annealed at 800 °C: single-phase composition (3), two-phase composition (4).

melting temperatures, and melting enthalpies of two eutectics were determined. The phase diagram of the NdF_3–Nd_2S_3 system was constructed. No noticeable solid solutions based on all NdF_3, NdSF, Nd_2S_3 compounds were formed in the system. The phase compositions of the samples were established for all phase-equilibrium fields. The liquidus of the system calculated from the Redlich–Kister equation is fully consistent with the DSC data.

The established physicochemical characteristics of NdSF and the NdF_3–Nd_2S_3 system can be used to study the $NdSF:Eu^{2+}$, $NdSF:Yb^{3+}$, and NdSF:P doping.

Our simulation experience also suggests that the option of absorption spectrum calculation, as implemented in the CASTEP package, is very useful. Some limitation of the CASTEP package is that no agreement could be obtained between simulated and experimental absorption values within a broad energy range (down to 25 eV or more). Combining the CASTEP advantages with those of modern simulation methods would be desirable for a more profound investigation of the solid-state absorption spectra formation.

Funding

CRediT authorship contribution statement

V.M. Grigorchenko: Writing – review & editing, Investigation, Conceptualization. **M.S. Molokeev:** Software, Formal analysis, Data curation. **A.S. Oreshonkov:** Software, Data curation. **A.S. Aleksandrovsky:** Writing – review & editing, Software, Formal analysis, Data curation. **A.V. Kertman:** Writing – original draft, Validation, Supervision. **M.U. Abulkhaev:** Writing – original draft, Visualization, Resources, Investigation. **A.S. Mereshchenko:** Validation, Supervision. **I.O. Yurev:** Writing – review & editing, Software, Data curation. **N.A. Shulaev:** Software, Formal analysis, Data curation. **D.N. Kamaev:** Software, Formal analysis, Data curation. **A.V. Elyshev:** Funding acquisition. **O.V. Andreev:** Writing – review & editing, Validation, Resources, Data curation.

Declaration of competing interest

Data availability

No data was used for the research described in the article.

Appendix A. Supplementary data

Supplementary data to this article can be found online at https://doi. org/10.1016/j.jssc.2024.124640.

References

[1] T. Arai, S. Iimura, H. Hosono, Doping induced polymorph and carrier polarity changes in LaSeF, Chem. Mater. 30 (2018) 597–601, https://doi.org/10.1021/acs. chemmater.7b05161.

[2] X. Goubin, X. Rocquefelte, D. Pauwels, A. Tressaud, A. Demourgues, S. Jobic, Y. Montardi, The dielectric function of LnSF rare-earth fluorosulfides (Ln= La, Ce): experiment and theory, J. Solid State Chem. 177 (2004) 2833–2840, https://doi. org/10.1016/j.jssc.2004.05.006.

[3] M.U. Abulkhaev, M.S. Molokeev, A.S. Oreshonkov, A.S. Aleksandrovsky, A. V. Kertman, D.N. Kamaev, O.V. Trofimova, A.V. Elyshev, O.V. Andreev, Properties of GdSF and phase diagram of the GdF_3 - Gd_2S_3 system, J. Solid State Chem. 322 (2023) 123991, https://doi.org/10.1016/j.jssc.2023.123991.

[4] P. Andreev, O. Mikhalkina, O. Andreev, A. Elyshev, Enthalpies of melting of LnSF compounds (Ln= La, Ce, Pr, Nd, Sm), Russ. J. Phys. Chem. A 89 (2015) 731–736, https://doi.org/10.1134/s0036024415050040.

[5] C. Buyer, H. Grossholz, S. Wolf, D. Zagorac, J. Zagorac, J.C. Schön, T. Schleid, Crystal-structure prediction and experimental investigation of the polymorphic lanthanum fluoride selenides LaFSe and La_2F_4Se, Cryst. Growth Des. 22 (2022) 7133–7142, https://doi.org/10.1021/acs.cgd.2c00810.

[6] D. Pauwels, A. Demourgues, A. Tressaud, Design and optical properties of rare earth-based mixed-anions (O,S,F) compounds, MRS Online Proc. Libr. OPL. 755 (2002), https://doi.org/10.1557/PROC-755-DD7.8.

[7] D. Pauwels, A. Demourgues, H. Laronze, P. Gravereau, F. Guillen, O. Isnard, A. Tressaud, Structural features of new rare earth-based mixed anions (O, S, F) compounds: relationships between optical absorption and rare earth environment, Solid State Sci. 4 (2002) 1471–1479, https://doi.org/10.1016/S1293-2558(02) 00038-9.

[8] A. Demourgues, A. Tressaud, H. Laronze, P. Gravereau, P. Macaudière, Preparation and structural properties of new series of mixed-anion compounds: rare earth fluorosulfides, J. Fluor. Chem. 107 (2001) 215–221, https://doi.org/10.1016/ S0022-1139(00)00361-4.

[9] P. Reynders, S. Bertaux, J.-U. Wichmann, Pearlescent Pigments Based on Fluorides, Oxyfluorides, Fluorosulfides And/or Oxyfluorosulfides, US20040219116A1, 2004. https://patents.google.com/patent/US20040219116A1/en. (Accessed 30 October 2023).

[10] J.M. Tomczak, L.V. Pourovskii, L. Vaugier, A. Georges, S. Biermann, Rare-earth vs. heavy metal pigments and their colors from first principles, Proc. Natl. Acad. Sci. USA 110 (2013) 904–907, https://doi.org/10.1073/pnas.1215066110.

[11] A. Demourgues, A. Tressaud, H. Laronze, P. Macaudière, Rare earth fluorosulfides LnSF and $Ln_2AF_4S_2$ as new colour pigments, J. Alloys Compd. 323–324 (2001) 223–230, https://doi.org/10.1016/S0925-8388(01)01116-1.

[12] L. Brixner, G. Hyatt, Precision lattice constants of the rare earth sulfofluorides of the type LnSF, Mater. Res. Bull. 19 (6) (1984) 745–750. https://doi:10.1016/0025-5408(84)90031-x.

[13] Y. Furuya, H. Tanaka, N. Kawaguchi, N. Abe, Y. Yokota, T. Yanagida, A. Yoshikawa, Crystal Growth and Scintillation Properties of NdF_3 Single Crystal, IEEE Nucl. Sci. (NSS/MIC), 2009, https://doi.org/10.1109/nssmic.2009.5402301.

[14] C. Li, P. Yang, Z. Xu, G. Li, D. Yang, C. Peng, J. Lin, others, Fine structural and morphological control of rare earth fluorides REF_3 (RE= La–Lu, Y) nano/microcrystals: microwave-assisted ionic liquid synthesis, magnetic and luminescent

properties, CrystEngComm 13 (2011) 1003–1013, https://doi.org/10.1039/C0CE00186D.

[15] F.H. Spedding, D.C. Henderson, High-temperature heat contents and related thermodynamic functions of seven trifluorides of the rare earths: Y, La, Pr, Nd, Gd, Ho, and Lu, J. Chem. Phys. 54 (1971) 2476–2483, https://doi.org/10.1063/1.1675202.

[16] T. Schleid, F. Lissner, Einkristalle von A-Nd_2S_3, U-Ho_2S_3, D-Er_2S_3 und E-Lu_2S_3, durch Oxidation reduzierter Chloride der Lanthanide mit Schwefel, Z. Anorg. Allg. Chem. 615 (1992) 19–26, https://doi.org/10.1002/zaac.19926150905.

[17] S. Osseni, P. Andreev, A. Polkovnikov, B. Zakharov, A. Aleksandrovsky, M. Abulkhaev, S. Volkova, D. Kamaev, I. Kovenskiy, N. Nesterova, others, Properties of oxysulfide phases and phase diagram of the Nd_2S_3–Nd_2O_3 system, J. Solid State Chem. 314 (2022) 123438, https://doi.org/10.1016/j.jssc.2022.123438.

[18] M. Shtykova, M. Molokeev, B. Zakharov, N. Selezneva, A. Aleksandrovsky, R. Bubnova, D. Kamaev, A. Gubin, N. Habibullayev, A. Matigorov, others, Structure and properties of phases in the $Cu_{2-X}Se$-Sb_2Se_3 system. The $Cu_{2-X}Se$-Sb_2Se_3 phase diagram, J. Alloys Compd. 906 (2022) 164384, https://doi.org/10.1016/j.jallcom.2022.164384.

[19] I.A. Razumkova, N.O. Azarapin, The nature of the interaction of $RE(NO_3)_3$ (yttrium subgroup) with HF or NH_4F, Z. Anorg. Allg. Chem. 647 (2021) 20–21, https://doi.org/10.1002/zaac.202100241.

[20] I.A. Razumkova, Y.G. Denisenko, A.N. Boyko, D.A. Ikonnikov, A. S. Aleksandrovsky, N.O. Azarapin, O.V. Andreev, Synthesis and upconversion luminescence in LaF_3: Yb^{3+}, Ho^{3+}, GdF_3: Yb^{3+}, Tm^{3+} and YF_3: Yb^{3+}, Er^{3+} obtained from sulfide precursors, Z. Anorg. Allg. Chem. 645 (2019) 1393–1401, https://doi.org/10.1002/zaac.201900204.

[21] I.A. Razumkova, A.N. Boiko, O.V. Andreev, S.A. Basova, Synthesis of [(H_3O) Tm_3F_{10}] nH_2O, ErF_3, and TmF_3 powders and their physicochemical properties, Russ. J. Inorg. Chem 62 (4) (2017) 418–422, https://doi.org/10.1134/s0036023617040155.

[22] P.O. Andreev, A.A. Polkovnikov, Y.G. Denisenko, O.V. Andreev, T.M. Burkhanova, A.N. Bobylev, L.A. Pimneva, Temperatures and enthalpies of melting of Ln_2S_3 (Ln= Gd, Tb, Dy, Ho, Er, Tm, Yb, and Lu) compounds, J. Therm. Anal. Calorim. 131 (2018) 1545–1551, https://doi.org/10.1007/s10973-017-6620-x.

[23] M. Ohta, S. Hirai, H. Kato, V.V. Sokolov, V.V. Bakovets, Thermal decomposition of NH_4SCN for preparation of Ln_2S_3 (Ln=La and Gd) by sulfurization, Mater. Trans. 50 (7) (2009) 1885–1889, https://doi.org/10.2320/matertrans.M2009060.

[24] R. Mauricot, P. Gressier, M. Evain, R. Brec, Comparative study of some rare earth sulfides: doped γ-[A] M_2S_3 (M = La, Ce and Nd, A = Na, K and Ca) and undoped γ-M_2S_3 (M = La, Ce and Nd), J. Alloys Compd. 223 (1) (1995) 130–138, https://doi.org/10.1016/0925-8388(94)01476-0.

[25] I. Vasil'eva, Y. Malovitsky, V. Kosyakov, Phase equilibrium and growth of homogeneous crystals in the γLa_2S_3 - γNd_2S_3 system, Mater. Res. Bull. 18 (1983) 1121–1127, https://doi.org/10.1016/0025-5408(83)90155-1.

[26] Degen, M. Sadki, E. Bron, U. König, G. Nénert, The HighScore suite, Powder Diffr. 29 (2014) S13–S18, https://doi.org/10.1017/s0885715614000840.

[27] S. Gates-Rector, T. Blanton, The Powder Diffraction File: a quality materials characterization database, Powder Diffr. 34 (2019) 352–360, https://doi.org/10.1017/S0885715619000812.

[28] A. Merkys, A. Vaitkus, A. Grybauskas, A. Konovalovas, M. Quirós, S. Gražulis, Graph isomorphism-based algorithm for cross-checking chemical and crystallographic descriptions, J. Cheminf. 15 (2023) 25, https://doi.org/10.1186/s13321-023-00692-1.

[29] A. Vaitkus, A. Merkys, S. Gražulis, Validation of the crystallography open database using the crystallographic information framework, J. Appl. Crystallogr. 54 (2021) 661–672, https://doi.org/10.1107/S1600576720016532.

[30] M. Quirós, S. Gražulis, S. Girdzijauskaitė, A. Merkys, A. Vaitkus, Using SMILES strings for the description of chemical connectivity in the Crystallography Open Database, J. Cheminf. 10 (2018) 23, https://doi.org/10.1186/s13321-018-0279-6.

[31] A. Merkys, A. Vaitkus, J. Butkus, M. Okulič-Kazarinas, V. Kairys, S. Gražulis, COD::CIF::Parser : an error-correcting CIF parser for the Perl language, J. Appl. Crystallogr. 49 (2016) 292–301, https://doi.org/10.1107/S1600576715022396.

[32] S. Gražulis, A. Merkys, A. Vaitkus, M. Okulič-Kazarinas, Computing stoichiometric molecular composition from crystal structures, J. Appl. Crystallogr. 48 (2015) 85–91, https://doi.org/10.1107/S1600576714025904.

[33] S. Gražulis, A. Daškevič, A. Merkys, D. Chateigner, L. Lutterotti, M. Quirós, N. R. Serebryanaya, P. Moeck, R.T. Downs, A. Le Bail, Crystallography Open Database (COD): an open-access collection of crystal structures and platform for world-wide collaboration, Nucleic Acids Res. 40 (2012) D420–D427, https://doi.org/10.1093/nar/gkr900.

[34] S. Gražulis, D. Chateigner, R.T. Downs, A.F.T. Yokochi, M. Quirós, L. Lutterotti, E. Manakova, J. Butkus, P. Moeck, A. Le Bail, Crystallography Open Database – an open-access collection of crystal structures, J. Appl. Crystallogr. 42 (2009) 726–729, https://doi.org/10.1107/S0021889809016690.

[35] R.T. Downs, M. Hall-Wallace, The American Mineralogist crystal structure database, Am. Mineral. 88 (2003) 247–250. https://pubs.geoscienceworld.org/msa/ammin/article-abstract/88/1/247/43886.

[36] Y.G. Denisenko, V.V. Atuchin, M.S. Molokeev, A.E. Sedykh, N.A. Khritokhin, A. S. Aleksandrovsky, A.S. Oreshonkov, N.P. Shestakov, S.V. Adichtchev, A. M. Pugachev, et al., Exploration of the crystal structure and thermal and spectroscopic properties of monoclinic praseodymium sulfate $Pr_2(SO_4)_3$, Molecules 27 (2022) 3966, https://doi.org/10.3390/molecules27133966.

[37] E.I. Sal'nikova, YuG. Denisenko, I.E. Kolesnikov, E. Lähderanta, O.V. Andreev, N. O. Azarapin, S.A. Basova, A.A. Gubin, A.S. Oreshonkov, Synthesis and luminescent properties of $(RE_{0.95}Ln_{0.05})_2O_2S$ (RE = La, Y; Ln = Ho, Tm), J. Solid State Chem. 293 (2020) 121753, https://doi.org/10.1016/j.jssc.2020.121753.

[38] L. Pimneva Andreev, Y_2S_3–Y_2O_3 phase diagram and the enthalpies of phase transitions, J. Solid State Chem. 263 (2018) 24–29, https://doi.org/10.1016/j.jssc.2018.03.001.

[39] M.A. Shtykova, V.P. Vorob'eva, P.P. Fedorov, M. Molokeev, A. Aleksandrovsky, A. Elyshev, I. Palamarchuk, I. Yurev, A. Ivanov, N. Habibullayev, others, Features of phase equilibria and properties of phases in the Sb-Sm-Se system, J. Solid State Chem. (2022) 123573, https://doi.org/10.1016/j.jssc.2022.123573.

[40] I.O. Yurev, A.S. Aleksandrovsky, D.N. Kamaev, A.A. Polkovnikov, V. M. Grigorchenko, A.A. Yarovenko, A.E. Zelenaya, M.D. Parfenova, O.V. Andreev, The Sm_2S_{3-x}-SmS-Sm_2O_2S refractory system: thermal analysis, phase diagram, and properties of the phases, J. Therm. Anal. Calorim. (2024), https://doi.org/10.1007/s10973-023-12792-z.

[41] S. Landi, I.R. Segundo, E. Freitas, et al., Use and misuse of the Kubelka–Munk function to obtain the band gap energy from diffuse reflectance measurements, Solid State Commun. 341 (2022) 114573, https://doi.org/10.1016/j.ssc.2021.114573.

[42] S. Rampino, F. Pattini, M. Bronzoni, et al., $CuSbSe_2$ thin film solar cells with ~4% conversion efficiency grown by low-temperature pulsed electron deposition, Sol. Energy Mater. Sol. Cells 185 (2018) 86–96, https://doi.org/10.1016/j.solmat.2018.05.024.

[43] N.N. Habibullayev, N.G. Naumov, A.N. Lavrov, N.V. Kuratieva, A. S. Aleksandrovsky, A.S. Oreshonkov, M.S. Molokeev, I.V. Palamarchuk, I.O. Yurev, Y.G. Denisenko, et al., Magnetic, optical, and thermic properties of $SrLnCuSe_3$ (Ln = Dy, Ho, Er, Tm) compounds, Magnetochemistry 9 (194) (2023), https://doi.org/10.3390/magnetochemistry9080194.

[44] S.J. Clark, M.D. Segall, C.J. Pickard, P.J. Hasnip, M.I.J. Probert, K. Refson, M. C. Payne, First principles methods using CASTEP, Z. Kristallogr. 220 (2005) 567–570, https://doi.org/10.1524/zkri.220.5.567.65075.

[45] M. Cococcioni, S. de Gironcoli, Linear response approach to the calculation of the effective interaction parameters in the LDA+U method, Phys. Rev. B 71 (2005) 035105, https://doi.org/10.1103/PhysRevB.71.035105.

[46] A.P. Bartók, J.R. Yates, Regularized SCAN functional, J. Chem. Phys. 150 (2019) 161101, https://doi.org/10.1063/1.5094646.

[47] N. Golovnev, M. Molokeev, Crystal structure of catena-(2-thiobarbiturato) dithallium (I), J. Struct. Chem. 55 (2014) 125–129.

[48] A. Galler, J. Boust, A. Demourgues, S. Biermann, L.V. Pourovskii, Correlated electronic structure and optical response of rare-earth based semiconductors, Phys. Rev. B 103 (2021) L241105, https://doi.org/10.1103/PhysRevB.103.L241105.